

An estimate of the local ISW signal, and its impact on CMB anomalies

Caroline L. Francis and John A. Peacock^{*}

SUPA† *Institute for Astronomy, University of Edinburgh, Blackford Hill, Edinburgh EH9 3HJ, UK.*

ABSTRACT

We estimate the local density field in redshift shells to a maximum redshift of $z = 0.3$, using photometric redshifts for the 2MASS galaxy catalogue, matched to optical data from the SuperCOSMOS galaxy catalogue. This density-field map is used to predict the Integrated Sachs-Wolfe (ISW) CMB anisotropies that originate within the volume at $z < 0.3$. We investigate the impact of this estimated ISW foreground signal on large-scale anomalies in the WMAP CMB data. We find that removal of the foreground ISW signal from WMAP data reduces the significance of a number of reported large-scale anomalies in the CMB, including the low quadrupole power and the apparent alignment between the CMB quadrupole and octopole.

Key words:

1 INTRODUCTION

The possible presence of non-Gaussian features in the low-order multipoles of the Cosmic Microwave Background has been a recurring theme in cosmology for over a decade. Large-scale anomalies of varying significance have been claimed, including the low power in the CMB quadrupole (Hinshaw et al. 1996; Spergel et al. 2003); the planarity of the octopole and its apparent alignment with the quadrupole (Tegmark et al. 2003; de Oliveira-Costa et al. 2004); the north-south power asymmetry about the ecliptic plane (e.g. Eriksen et al. 2004) and the extension of the $\ell = 2$ and $\ell = 3$ alignments to higher multipoles (Schwarz et al. 2004; Copi et al. 2006), defining the ‘Axis of Evil’ (Land & Magueijo 2005). A closely related result is the lack of large-angle correlations in the CMB sky (Hinshaw et al. 1996; Copi et al. 2009). On smaller scales, Vielva et al. (2004) suggest that the CMB contains a non-Gaussian ‘cold spot’ in the southern hemisphere. There are four possible explanations for these CMB anomalies: (i) a problem with the data; (ii) an unlucky fluke; (iii) new early-universe physics; or (iv) they are due to a foreground signal. Here we explore the last of these possibilities.

The ISW effect is a secondary anisotropy in the CMB caused by the passage of CMB photons through evolving gravitational potential wells:

$$\frac{\Delta T^{\text{ISW}}}{T_{\text{CMB}}} = 2 \int_{t_{\text{LS}}}^{t_0} \frac{\dot{\Phi}(\vec{x}(t), t)}{c^2} dt, \quad (1)$$

where t_0 and t_{LS} denote the times today and at last scattering respectively; \vec{x} is the position along the line of sight of the photon at time t and Φ is the gravitational potential (Martinez-Gonzalez et al. 1990). On large scales in a Dark Energy dominated universe, CMB photons gain energy when they pass through the decaying potential wells associated with overdensities and lose energy on passing through underdensities. This leads to the large-scale positive cross-correlation between large scale structure and the CMB that is often used to attempt detections of the ISW effect (Crittenden & Turok 1996).

The ISW effect is the only significant secondary CMB anisotropy at low ℓ . The only other non-negligible signal, due to the thermal SZ effect, is approximately an order of magnitude smaller than the expected ISW signal. Our aim here is to predict the local ISW signal to a maximum redshift of $z = 0.3$ and consider the effect of removing this part of the foreground signal on the large-scale CMB anomalies. The data and method used to predict the local ISW signal are described in Section 2 and the effect of this foreground signal on large-scale CMB anomalies is explored in Section 3. Finally, our conclusions are presented in Section 4. A cosmological model with $\Omega_m = 0.3$, $\Omega_v = 0.7$, $\Omega_b = 0.05$, $h = 0.7$ and $\sigma_8 = 0.75$ is assumed unless otherwise stated.

2 PREDICTION OF THE LOCAL ISW SIGNAL

In order to predict the local ISW signal, it is first necessary to estimate the density field within the volume of interest. We make a 2D Wiener reconstruction of the projected density field in redshift shells, using photometric redshift data

^{*} E-mail: jap@roe.ac.uk

† Scottish Universities Physics Alliance

for the 2MASS galaxy catalogue. An account of the data and method used for this reconstruction is given in Section 2.1 and the estimation of the local ISW signal from this density field is described in Section 2.2.

2.1 Recovery of the local density field

2.1.1 Data

The 2MASS dataset used in this paper is described briefly below. This material is common to a companion paper about attempted detection of the ISW effect via cross-correlation (Francis & Peacock 2009) and fuller details are given there.

2MASS is an all-sky survey in the J , H and K_s bands (Jarrett 2004). This near-infrared selection means that 2MASS is sensitive to old stars and hence to the most massive structures, which makes it well-suited for constructing maps of galaxy mass density. The final extended source catalogue (XSC) contains over 1.6 million objects, over 98% of which are galaxies. Photometric redshifts for the 2MASS XSC have been generated by matching the 2MASS data with optical catalogues from SuperCOSMOS scans of major photographic sky surveys (UKST in the south; POSS2 in the north) to create a 5-band *BRJHK* dataset. Details of the SuperCOSMOS catalogue construction process are given in Hambly et al. (2001) and details of the photometric calibration and photo- z determination method are given in Peacock et al. (2010). The final photometric redshift dataset has an overall rms in $z_{\text{phot}} - z$ of 0.033.

A magnitude cut $K_s < 13.8$ is imposed on the extinction-corrected data to ensure uniformity across the region outside the Galactic plane. The Galactic plane mask is constructed using the dust maps of Schlegel et al. (1998) and excludes all regions with K -band reddening $A_K > 0.05$. This leaves approximately 67% of the sky unmasked. Whilst the choice of $A_K > 0.05$ is conservative, Afshordi et al. (2004) note that the number density within pixels of faint galaxies ($13.5 < K_{20} < 14.0$) drops off as a function of A_K for $A_K > 0.065$. A less conservative mask, for example with $A_K > 0.1$, would still only leave 79% of the sky unmasked – at the price of possible incompleteness issues in the analysis.

2.1.2 Density field reconstruction

It is possible to attempt a full 3D reconstruction of the local density field with this photometric redshift dataset, and then use this to estimate the local ISW signal (see Francis 2008). However, this recovered density field is subject to significant radial smearing due to the uncertainty in the radial position of each galaxy (approximately $100 h^{-1} \text{Mpc}$). The extent of this smearing justifies a simpler and more transparent approach: to recover the projected density field for 3 thick redshift slices of width $\Delta z = 0.1$ to $z_{\text{max}} = 0.3$, and estimate the ISW signal due to each slice.

The galaxy distribution in each photometric redshift shell is known outside the masked region. We use a Wiener filtering technique to recover the galaxy density field in each shell. When the Wiener filter is applied to all-sky data, it recovers the optimal density field in the least squares sense; a thorough discussion of Wiener-filter density reconstruction is presented in e.g. Zaroubi et al. (1995).

Because our dataset is masked at low Galactic latitudes,

the simple all-sky Wiener approach must be modified. We proceed by initially filling the masked region in each of the redshift shells with a random Poisson sampling of galaxies according to the average number density observed outside the plane. This galaxy distribution is then used to deduce the projected galaxy density field for the redshift shell. The Wiener filter appropriate for each shell is then constructed as usual:

$$\Phi_{\text{WF}}(\ell) = \frac{C_{\text{gg}}(\ell)}{C_{\text{gg}}(\ell) + C_{\text{noise}}(\ell)}, \quad (2)$$

where $C_{\text{gg}}(\ell)$ is the angular power spectrum of galaxies in that redshift shell and $C_{\text{noise}}(\ell)$ describes shot noise. The Wiener filter is applied in the first instance to the $a_{\ell m}$ coefficients computed for the expansion of this initial full-sky galaxy density field into a basis of spherical harmonics. The resultant density field within the masked region is Poisson sampled for galaxies once more to yield a revised galaxy distribution composed of a sample from the Wiener reconstruction within the plane, and the original 2MASS galaxies in the unmasked regions. In this way, large-scale features in surface density can be extrapolated across the plane in a consistent way. The process can be iterated, but this did not yield a significant improvement in the final results. We have carried out tests of this method on simulated data, and find satisfactory recovery of the estimated ISW signal (Francis 2008). Fig. 1 shows the recovered projected density field for each of the three shells. We use HEALPix software (Gorski et al. 2005; see also <http://healpix.jpl.nasa.gov>) to generate these maps and to perform harmonic analysis of them.

2.2 Prediction of the local ISW signal

Given a projected galaxy density field in a thick redshift shell, it is possible to estimate the CMB temperature fluctuations, ΔT , due to the ISW effect. Poisson's equation tells us the time variation of the potential field in terms of the density growth factor in the linear regime, $g(a)$:

$$\Phi(a) = \frac{g(a)}{a} \Phi(a = 1). \quad (3)$$

Hence, using Poisson's equation, we can integrate through a shell of thickness Δr :

$$\begin{aligned} \frac{\Delta T_{\ell m}}{T} &= -2 \int \frac{d}{dt} \left[\frac{g(a)}{a} \right] \frac{a^2 \Phi_{\ell m}(a)}{g(a)} \frac{dr}{c^3} \\ &\simeq \frac{-2}{c^3} H(\bar{a}) \left(\frac{dg}{da}(\bar{a}) - \frac{g(\bar{a})}{\bar{a}} \right) \frac{\bar{a}^2}{g(\bar{a})} \int \Phi_{\ell m} dr \\ &\simeq \frac{3H_0^2 \Omega_m}{\ell(\ell+1)c^3} \left(1 - \bar{a} \frac{g'(\bar{a})}{g(\bar{a})} \right) r^2(\bar{a}) H(\bar{a}) \frac{\delta_{\ell m}}{b} \Delta r, \end{aligned} \quad (4)$$

where δ is the projected galaxy density field in the redshift shell under consideration and $\bar{a} = (1 + \bar{z})^{-1}$ with \bar{z} the redshift at the midpoint of the shell. The bias in each redshift shell between the galaxy and matter density fields is approximated using a linear bias relation $\delta_g = b\delta_m$ and is assumed to be independent of scale and redshift in each shell. To deduce the appropriate value of b in each redshift shell, a maximum likelihood fit of the predicted galaxy angular power spectrum to the measured galaxy angular power spectrum is performed as in Francis & Peacock (2009).

Fig. 1 shows the results of estimating the local ISW effect from the Wiener filtered density field in redshift shells.

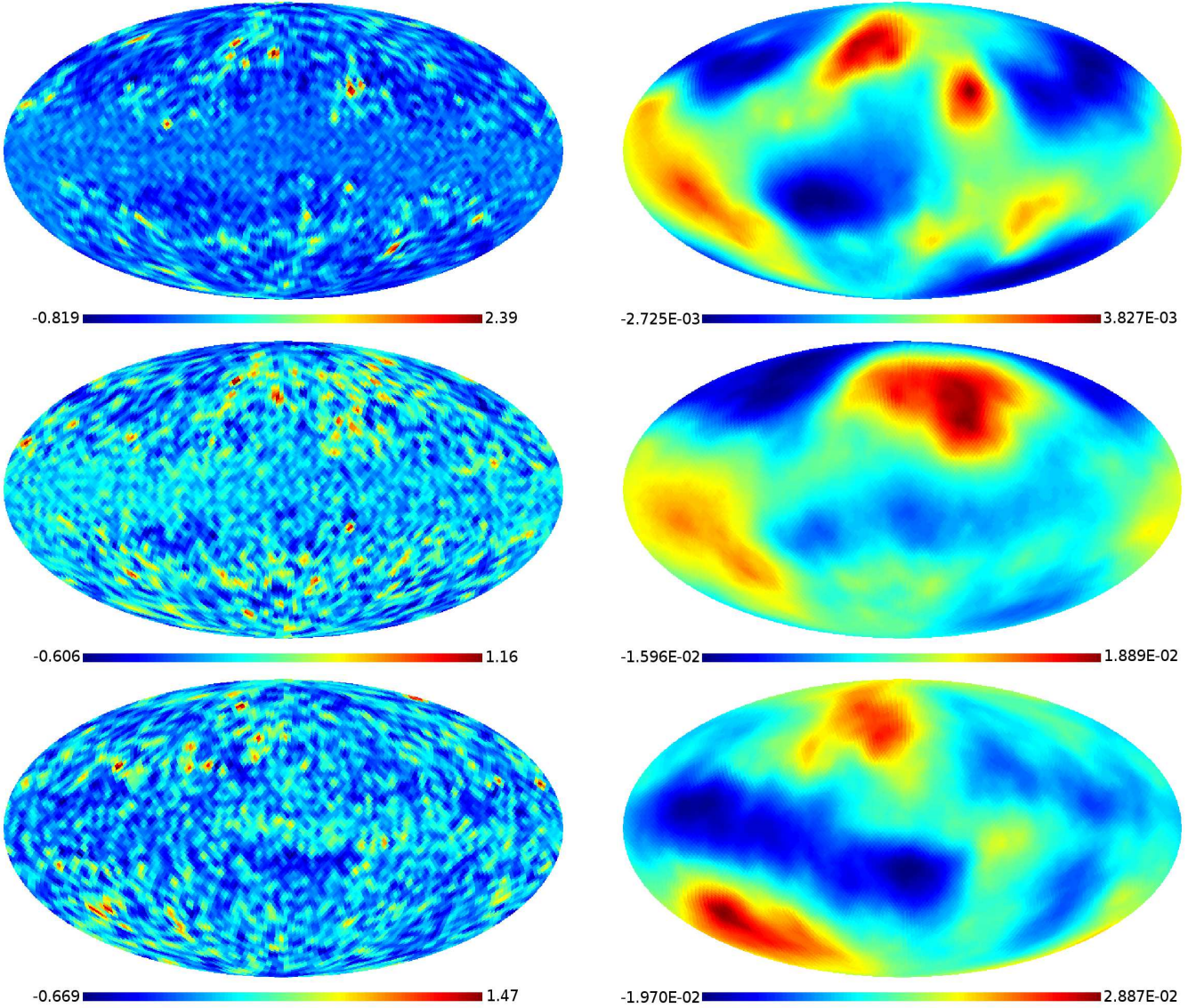


Figure 1. (Left) The 2D reconstruction of the local density field described in Section 2.1 in three photometric redshift shells: $0.0 < z < 0.1$ (top), $0.1 < z < 0.2$ (middle) and $0.2 < z < 0.3$ (bottom). The plots show overdensity δ on a scale $-0.6 \leq \delta \leq 0.6$. (Right) The corresponding ISW signal in mK computed from the reconstructed density field using equation (4).

These ISW maps are affected by overlap effects due to the uncertainty in the radial position of each galaxy: galaxies associated with an overdensity near the boundary of a shell will to some extent be spread across both the ‘true’ shell and the adjacent redshift shell. Fig. 2 shows the angular power spectrum of the ISW signal in each slice, together with the predicted linear ISW signal. For these predictions, we have accounted for the smearing effects of the photometric redshift data by assuming that photo- z ’s apply Gaussian smoothing along the radial axis with $\sigma_r = 90 h^{-1} \text{Mpc}$. Fig. 2 also shows the effect of this radial smearing on the total predicted ISW signal to $z_{\text{max}} = 0.3$. Overall, the agreement between observed and predicted power spectra is good, which illustrates that the effect of photo- z imperfection is relatively minor for $\ell \lesssim 20$.

We note that the estimated ISW signal in the lower two redshift slices is slightly larger than expected at $\ell \gtrsim 20$; this is particularly noticeable in the $z < 0.1$ slice. The nonlin-

ear Rees-Sciama effect is expected to increase the power at high ℓ , doubling the power at $\ell \simeq 200$ (e.g. Cooray & Sheth 2002). Since the mean depth of the lowest-redshift shell is of order one tenth of the distances that dominate the total ISW effect, it is plausible that we are seeing some local Rees-Sciama effect. In any case, the main focus of the present paper is at larger angular scales. We also note that the estimated ISW power is larger than expected for $\ell \lesssim 3$ in the $0.1 < z < 0.2$ shell and for $\ell \lesssim 5$ in the $0.2 < z < 0.3$ shell, which leads to a larger than average total signal for $z_{\text{max}} = 0.3$ on such scales. Such small- ℓ modes are potentially sensitive to the corrections for mask incompleteness near the plane, but tests of our method on mock data show no tendency to bias the power high in this regime (although it does increase the already considerable cosmic variance). Any discrepancy is relative to our standard model of $\Omega_m = 0.3$, which is perhaps on the high-density side given current data (Komatsu et al. 2009). Decreasing Ω_m

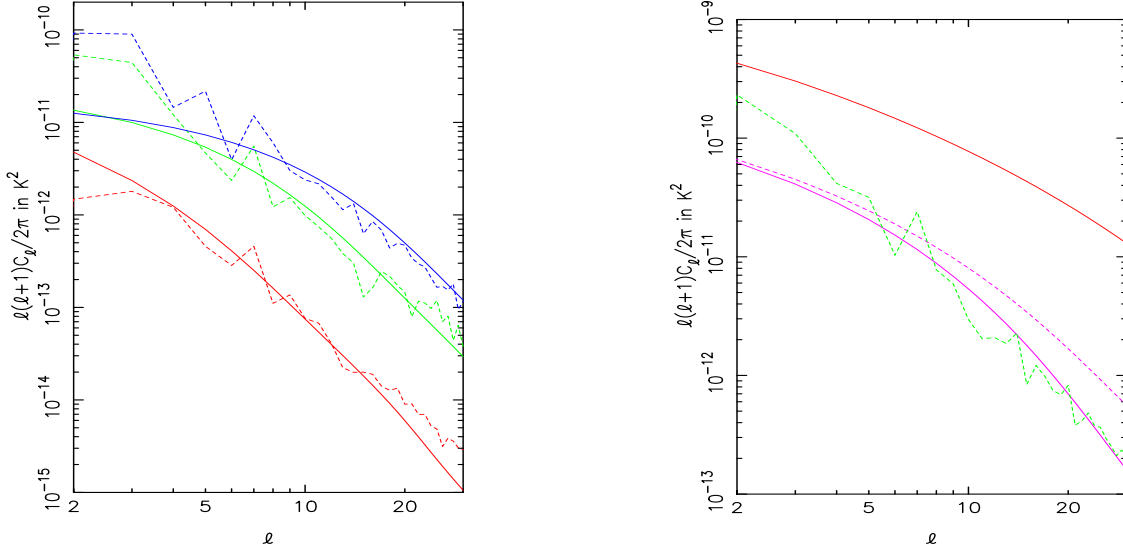


Figure 2. (Left) The power spectrum of the ISW signal estimated in each of the three redshift shells (dashed lines): $0.0 < z < 0.1$ (bottom), $0.1 < z < 0.2$ (middle) and $0.2 < z < 0.3$ (top) together with the predicted signal for $\Omega_m = 0.3$ (solid lines), allowing for radial smearing. (Right) The predicted total ISW power for $z_{\text{max}} \rightarrow \infty$ (upper red solid line) and for $z_{\text{max}} = 0.3$ (middle purple dashed line) and that expected for $z_{\text{max}} = 0.3$ allowing for radial smearing (lower purple solid line). The green dashed line shows the power spectrum measured for the estimated $z_{\text{max}} = 0.3$ ISW signal.

to 0.25 with other parameters held fixed raises the expected quadrupole power for $z_{\text{max}} = 0.3$ by a factor 1.5; our adopted normalization of $\sigma_8 = 0.75$ might also be increased, so that the predicted low- ℓ ISW power could plausibly increase in amplitude by a factor 2. We will thus provisionally adopt the large-scale ISW map as estimated, but will also explore the consequences of scaling its amplitude down to the lower values expected in our $\Omega_m = 0.3$ model.

Fig. 2 also shows the total ISW signal for $z_{\text{max}} \rightarrow \infty$, which we can use to estimate the fraction of the total ISW signal that we expect to include if $z_{\text{max}} = 0.3$. The square root of the ratio of the predicted ISW power for $z_{\text{max}} \rightarrow \infty$ to that for $z_{\text{max}} = 0.3$ shows that we can expect to include $\sim 40\%$ of the total rms ISW temperature signal at low multipoles, falling to $\sim 10\%$ at $\ell = 30$. This variation with angular scale is mainly due to the greater importance of the high redshift ISW signal at large ℓ .

3 IMPLICATIONS FOR CMB ANOMALIES

Having made a prediction of the local ISW signal, we now investigate the effect of this foreground signal on a number of the large scale anomalies that have been reported in the CMB. Many of these CMB anomalies relate solely to the $\ell = 2$ and $\ell = 3$ multipoles and, as noted in Section 2.2, the estimated local ISW power is greater than the ensemble average on these scales. We therefore consider two versions of the estimated local ISW signal in this analysis of the CMB anomalies: the ISW prediction described in Section 2 and a rescaled version of this signal chosen to maintain the phases of the original signal but to have the power spectrum expected of the ISW signal out to $z = 0.3$ for our standard choice of $\Omega_m = 0.3$. Consideration of this latter ISW signal allows us to assess the possibility that any effect on the CMB anomalies is solely due to the large low-multipole power of the estimated ISW signal.

We now consider the effect of removing the local ISW signal on each of the large scale CMB anomalies. We use the year-3 WMAP ILC map (hereafter ILC) and the CMB map computed by de Oliveira-Costa & Tegmark (2006) from the year-3 WMAP data (hereafter OT). We have removed the kinetic Doppler dipole and quadrupole contributions due to the motion of the Sun with respect to the CMB frame.

3.1 Low quadrupole power

Figure 3 shows the $\ell = 2$ and $\ell = 3$ multipoles of the estimated local ISW signal, the WMAP ILC map and the WMAP ILC map after removal of the estimated ISW signal. We immediately note a significant increase in the temperature range of the quadrupole map after ISW removal and an alteration in the positions of the temperature extrema for this multipole; in contrast, the octopole is largely unchanged. We compute the power of the quadrupole for these maps, together with the foreground-cleaned map of de Oliveira-Costa & Tegmark (2006) before and after ISW subtraction. The results and their significance given the WMAP best-fitting model prediction are given in Table 1. We also repeat the exercise for the CMB maps with the rescaled version of the local ISW prediction removed. The results in Table 1 show that the low value of the quadrupole power ceases to be significant when we consider the maps with either the original or the rescaled versions of the estimated local ISW signal removed. This is one of the main results of this paper, and its broader significance is discussed in the concluding section.

3.2 Quadrupole/octopole alignment

In order to quantify the alignment between the quadrupole and octopole, we have used the maximum angular dispersion technique of de Oliveira-Costa et al. (2004) to identify

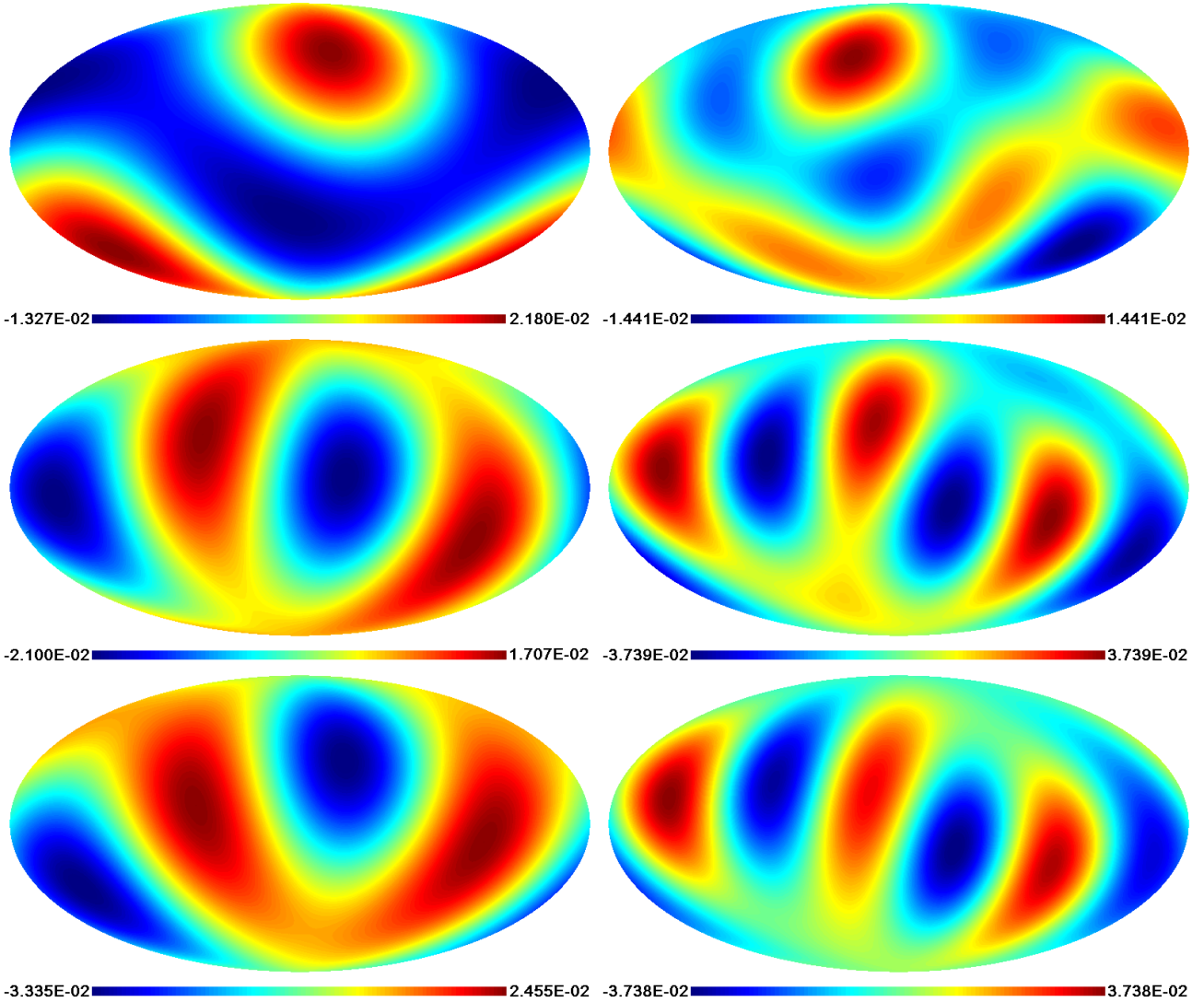


Figure 3. (Top) The quadrupole (left) and octopole (right) in mK of the estimated local ISW effect. (Centre) The quadrupole (left) and octopole (right) in mK of the WMAP ILC map. (Bottom) The quadrupole (left) and octopole (right) in mK of the ILC map after subtracting the local ISW contribution.

| Map | Quadrupole Power / μK^2 | Probability |
|----------------------|------------------------------------|-------------|
| ILC | 250.6 | 3.5% |
| OT | 214.3 | 2.4% |
| ILC – ISW | 600.7 | 19.8% |
| OT – ISW | 608.2 | 20.1% |
| ILC – ISW (rescaled) | 372.2 | 8.0% |
| OT – ISW (rescaled) | 358.8 | 7.5% |

Table 1. The quadrupole power for the WMAP ILC and OT maps before and after subtraction of the estimated local ISW signal for $z < 0.3$, together with its significance given the best-fitting year-3 WMAP prediction. This is a one-tailed probability of having a quadrupole as low or lower than observed, given the distribution of quadrupole power (χ^2 with 5 d.f.). We note that the quadrupole power is no longer unusually low after subtraction of the ISW signal.

preferred axes for the quadrupole, $\hat{\mathbf{n}}_2$, and octopole, $\hat{\mathbf{n}}_3$. Thus we search over directions $\hat{\mathbf{n}}$ to maximise the quantity

$\sum_m m^2 |a_{\ell m}|^2$ in a coordinate system with $\hat{\mathbf{n}}$ as the direction of the z -axis. Our results are given in Table 2. We see that there is no significant alignment remaining in either the ILC or OT map after removal of either the estimated local ISW signal or the rescaled version.

3.3 Planarity of the octopole

Fig. 3 shows that the octopole is not particularly affected by the subtraction of the estimated local ISW effect. Evaluating the ‘ t ’ statistic of de Oliveira-Costa et al. (2004)

$$t = \max_{\hat{\mathbf{n}}} \frac{|a_{3-3}|^2 + |a_{33}|^2}{\sum_m |a_{\ell m}|^2} \quad (5)$$

as a measure of planarity, we find the results given in Table 3. The significance of the ‘ t ’ statistic is evaluated by considering 10000 simulated sets of $a_{\ell m}$ data and determining the frequency of such ‘ t ’ values occurring by chance (see de Oliveira-Costa et al. 2004 for further details). The ISW

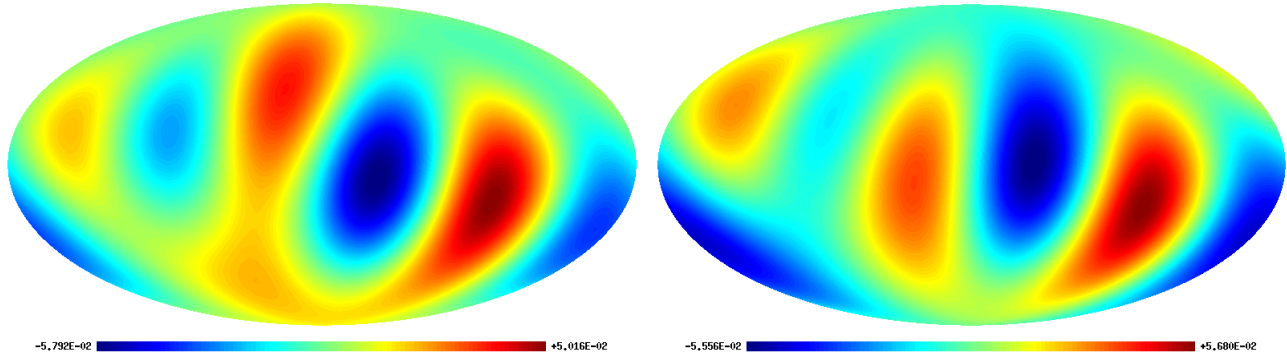


Figure 4. The $\ell = 2 + 3$ multipoles of the year-3 ILC map (left) and the ILC map after subtraction of the estimated local ISW signal (right) in mK; the black line shows the ecliptic plane. We note that the power asymmetry persists, with the largest temperature extrema seen south of the ecliptic plane, but that the ecliptic no longer lies along a node line of the temperature distribution.

| Map | $\hat{n}_2 \cdot \hat{n}_3$ | Separation | Probability |
|----------------------|-----------------------------|------------|-------------|
| ILC | 0.9991 | 2.4° | 0.09% |
| OT | 0.9881 | 8.9° | 1.2% |
| ILC – ISW | 0.7548 | 41.0° | 24.5% |
| OT – ISW | 0.6712 | 47.8° | 32.9% |
| ILC – ISW (rescaled) | 0.8888 | 27.3° | 11.1% |
| OT – ISW (rescaled) | 0.8183 | 35.1° | 19.2% |

Table 2. The scalar product of the preferred axes of the quadrupole and octopole together with their angular separation and the one-tailed probability of such a good separation occurring by random alignment. Results are shown for the ILC and OT maps before and after removal of both the estimated local ISW signal and the rescaled version.

| Map | t value | Probability |
|----------------------|-----------|-------------|
| ILC | 0.9213 | 17% |
| OT | 0.9269 | 15% |
| ILC – ISW | 0.9841 | 1.6% |
| OT – ISW | 0.9653 | 5.0% |
| ILC – ISW (rescaled) | 0.9661 | 4.9% |
| OT – ISW (rescaled) | 0.9524 | 8.0% |

Table 3. The t value for the octopoles of each of our usual maps together with the one-tailed probability of such an extreme value occurring by chance, as determined from 10000 Monte-Carlo simulations of a_{3m} coefficients. Removal of the estimated local ISW effect actually makes the octopole more planar.

subtracted maps have octopoles that are slightly more planar than the corresponding ILC or OT maps, i.e. removal of the estimated local ISW effect seems to make the octopole more planar. The probability of such planarity occurring by chance varies depending on the CMB map which is used, with probabilities of $\sim 2 - 5\%$ for the full local ISW subtraction and $\sim 5 - 8\%$ for the rescaled ISW subtraction.

3.4 North-South asymmetry

Fig. 4 shows the sum of the quadrupole and octopole for the ILC map, before and after ISW subtraction. An asymmetry in power between the hemispheres north and south of the ecliptic remains after removal of the estimated ISW signal,

but the ecliptic no longer lies along a null of the temperature distribution. The significance of the power asymmetry and the coincidence of the ecliptic with a node line across $1/3$ of the sky was found by Schwarz et al. (2004) to be unusual at the 95% level. We expect that the breaking of this coincidence with the ecliptic that occurs after ISW removal would reduce the significance of the anomaly much further.

3.5 Cold spot

The ‘cold spot’ is centred at $\ell = 207.8^\circ$, $b = -56.3^\circ$ and has scale $\sim 10^\circ$. This feature was identified by Vielva et al. (2004) using Spherical Mexican Hat Wavelets in the year-1 WMAP CMB data and confirmed in the year-3 WMAP data (Cruz et al. 2007). Rudnick et al. (2007) identified the region of the cold spot with an underdensity of NVSS radio sources and therefore suggested that the cold spot is due to the ISW contribution of a large void at redshift $z \sim 1$. However, Smith & Huterer (2010) find no evidence for such an underdensity of NVSS sources. We have evaluated the CMB temperature in the vicinity of the cold spot before and after the subtraction of the estimated local ISW signal; the pixels in the vicinity of the cold spot become on average $7\mu\text{K}$ warmer after ISW removal. This changes the formal significance level of the feature from 1.85% to 2.5%.

If the cold spot were due to the ISW contribution of a large void at $z \sim 1$, removal of the estimated local ISW signal slightly reduces the size of the necessary void to around 95% of the current estimate of about $105 h^{-1} \text{Mpc}$ at $z \simeq 1$ (Rudnick et al. 2007). A void of this size would remain anomalously large.

4 CONCLUSIONS

We have estimated the local ISW signal to $z = 0.3$ based on large scale structure data from 2MASS and SuperCOSMOS. On subtracting this predicted foreground from CMB data, we find that many large-scale CMB anomalies are alleviated. In particular the quadrupole power is raised and the alignment between the $\ell = 2$ and $\ell = 3$ multipoles is broken. We have checked that these results are not sensitive to the precise amplitude of the low multipoles of the estimated ISW signal by considering in addition a rescaled

version of the ISW map, chosen to have the same phases as the original estimation but a power spectrum equal to that expected for the local ISW effect with $\Omega_m = 0.3$. On subtraction of the estimated ISW foreground, we also find that the co-incidental alignment of the ecliptic with a node line of the $\ell = 2 + 3$ multipoles of the CMB is broken (although the north-south asymmetry in the signal remains) and that the temperature in the vicinity of the non-Gaussian cold spot is slightly raised (although the change in significance is not substantial). Of the large-scale anomalies considered, the planarity of the octopole remains most unusual, and in fact becomes more significant on removal of the ISW signal – but $\sim 5\%$ significance is hardly compelling evidence for any anomaly.

These results thus demonstrate that removal of the local ISW effect can mitigate the anomalous signals that have been claimed on large scales in the CMB. Our estimate of the CMB signal that originates at $z > 0.3$ has a character that is a better match to the expected Gaussian random field. The harmonic-space anomalies investigated here are closely related to the issue of lack of large-scale angular correlations, and one might expect that ISW subtraction would also remove this problem; Efstathiou et al. (2009) have used the data from the present paper to show that this is indeed the case.

It should be borne in mind that we have only considered the ISW signal for $0 < z < 0.3$ in this work, which we estimate to contain around 40% of the total rms ISW signal at low multipoles, and therefore there will be further substantial influence on the observed CMB from the ISW effect at higher redshifts: an upper limit of $z < 1.3$ would yield $> 90\%$ of the signal. Future imaging surveys will provide photometric redshifts to this depth (approximately an AB magnitude limit of $r = 24$), but extensive sky coverage will be hard to obtain; the Dark Energy Survey (DES Collaboration 2005) will cover 5000 deg^2 by about 2015, but the full extragalactic sky will probably have to await results from LSST (Ivezic et al. 2008) in perhaps 2020, or ultimately ESA’s Euclid mission (Laureijs 2009), which is currently scheduled to finish in about 2023.

Our work nevertheless demonstrates that it is important to estimate the contribution of ISW secondary anisotropies to the CMB before concluding that the large scale intrinsic CMB signal is anomalous or otherwise. In this respect, we agree with previous workers who have argued that foregrounds from large-scale structure might affect the CMB anomalies: Rakic et al. (2006) looked at the nonlinear Rees-Sciama effect and Abramo et al. (2006) the Sunyaev-Zeldovich effect. However, it is well established that the ISW signal is much the largest of these foregrounds on the relevant scales (e.g. Cooray & Sheth 2002), and so ISW removal should dominate any change in the character of the CMB sky.

Of course, it can be argued that we have replaced one puzzle by another: the intrinsic CMB should be statistically isotropic and Gaussian, and the large-angle ISW signal should very nearly have the same character. At the lowest multipoles, the prediction of the standard cosmology is that the power from each of these components should be very nearly equal (see Figure 62 from Cooray & Sheth 2002). How could the sum of two uncorrelated Gaussian fields *reduce* the total quadrupole power, and introduce non-

Gaussian correlations at higher multipoles? Within the standard model, such an outcome would have to be a fluke, and it is true that some authors (e.g. Efstathiou 2004) claim that the statistical significance of the claimed anomalies is not overwhelming.

If we reject the idea of a fluke, then either the intrinsic CMB or the foreground would have to be anomalous, unless a new mechanism can be found to correlate these two components. Regarding non-standard foregrounds, Gordon et al. (2005) showed that it is hard to produce the complete set of claimed anomalies by adding uncorrelated signals even if the foreground component is made explicitly anisotropic; rather, they claim that one would need a multiplicative anisotropy in which the temperature variance has a large-scale variation over the sky. At higher multipoles than considered here, there is accumulating evidence that just such an effect exists, with both a dipole and quadrupole modulation (e.g. Hanson & Lewis 2009; Hoftuft et al. 2009). If such effects are not low-level instrumental systematics, then a radical new ingredient in cosmological structure formation is required; but in either case, there is no evidence that these modulations have any relation to the claimed large-angle anomalies. Our position on these is that exotic mechanisms for explaining CMB anomalies as a real physical effect (e.g. Luminet et al. 2003), tend to apply only to the intrinsic anisotropies that originate at $z \simeq 1100$, so that we should try to isolate these from foreground emission as cleanly as possible. We have tried to perform this task in the present paper by removing part of the ISW foreground, with the result that the estimate of the intrinsic CMB no longer appears unusual in its large-scale properties. This reduces the motivation for revisions to the standard theory for the origin of CMB fluctuations, even if it leaves the door open for a more elaborate model that could introduce a correlation between the intrinsic CMB and foreground anisotropies.

ACKNOWLEDGEMENTS

CLF was supported by a PPARC PhD studentship. We thank Kate Land for much helpful correspondence. This research has made use of optical data obtained from the SuperCOSMOS Science Archive, prepared and hosted by the IfA’s Wide Field Astronomy Unit, consisting of scanned survey plates from the UK Schmidt Telescope and The Palomar Observatory Sky Survey (POSS-II). This publication also makes use of data products from the Two Micron All Sky Survey, which is a joint project of the University of Massachusetts and the Infrared Processing and Analysis Center/California Institute of Technology, funded by the National Aeronautics and Space Administration and the National Science Foundation.

REFERENCES

- Abramo L. R., Sodr e L. J., Wuensche C. A., 2006, Phys. Rev. D, 74, 083515
- Afshordi N., Loh Y.-S., Strauss M. A., 2004, Phys. Rev. D, 69, 083524
- Cooray A., Sheth R., 2002, Physics Reports, 372, 1

- Copi C. J., Huterer D., Schwarz D. J., Starkman G. D., 2006, MNRAS, 367, 79
- Copi C. J., Huterer D., Schwarz D. J., Starkman G. D., 2009, MNRAS, 399, 295
- Crittenden R. G., Turok N., 1996, Physical Review Letters, 76, 575
- Cruz M., Cayón L., Martínez-González E., Vielva P., Jin J., 2007, ApJ, 655, 11
- de Oliveira-Costa A., Tegmark M., 2006, Phys. Rev. D, 74, 023005
- de Oliveira-Costa A., Tegmark M., Zaldarriaga M., Hamilton A., 2004, Phys. Rev. D, 69, 063516
- DES Collaboration 2005, arXiv:astro-ph/0510346
- Efstathiou G., 2004, MNRAS, 348, 885
- Efstathiou G., Ma Y., Hanson D., 2009, arXiv:0911.5399
- Eriksen H. K., Hansen F. K., Banday A. J., Górski K. M., Lilje P. B., 2004, ApJ, 605, 14
- Francis C. L., 2008, PhD thesis, University of Edinburgh
- Francis C. L., Peacock J. A., 2009, arXiv:0909.2494
- Gordon C., Hu W., Huterer D., Crawford T., 2005, Phys. Rev. D, 72, 103002
- Górski K. M., Hivon E., Banday A. J., Wandelt B. D., Hansen F. K., Reinecke M., Bartelmann M., 2005, ApJ, 622, 759
- Hambly N. C., Davenhall A. C., Irwin M. J., MacGillivray H. T., 2001, MNRAS, 326, 1315
- Hanson D., Lewis A., 2009, Phys. Rev. D, 80, 063004
- Hinshaw G., Banday A. J., Bennett C. L., Gorski K. M., Kogut A., Lineweaver C. H., Smoot G. F., Wright E. L., 1996, ApJ, 464, L25
- Hoftuft J., Eriksen H. K., Banday A. J., Górski K. M., Hansen F. K., Lilje P. B., 2009, ApJ, 699, 985
- Ivezic Z., Tyson J. A., Allsman R., Andrew J., Angel R., for the LSST Collaboration 2008, arXiv:0805.2366
- Jarrett T., 2004, Publications of the Astronomical Society of Australia, 21, 396
- Komatsu E., et al., 2009, ApJS, 180, 330
- Land K., Magueijo J., 2005, Physical Review Letters, 95, 071301
- Laureijs R., 2009, arXiv:0912.0914
- Luminet J.-P., Weeks J. R., Riazuelo A., Lehoucq R., Uzan J.-P., 2003, Nature, 425, 593
- Martinez-Gonzalez E., Sanz J. L., Silk J., 1990, ApJ, 355, L5
- Peacock J. A., et al., 2010, in prep.
- Rakic A., Rasanen S., Schwarz D. J., 2006, MNRAS, 369, L27
- Rudnick L., Brown S., Williams L. R., 2007, ApJ, 671, 40
- Schlegel D. J., Finkbeiner D. P., Davis M., 1998, ApJ, 500, 525
- Schwarz D. J., Starkman G. D., Huterer D., Copi C. J., 2004, Physical Review Letters, 93, 221301
- Smith K. M., Huterer D., 2010, MNRAS, 403, 2
- Spergel D. N., et al., 2003, ApJS, 148, 175
- Tegmark M., de Oliveira-Costa A., Hamilton A. J., 2003, Phys. Rev. D, 68, 123523
- Vielva P., Martínez-González E., Barreiro R. B., Sanz J. L., Cayón L., 2004, ApJ, 609, 22
- Zaroubi S., Hoffman Y., Fisher K. B., Lahav O., 1995, ApJ, 449, 446

This paper has been typeset from a $\text{\TeX}/\text{\LaTeX}$ file prepared by the author.